Species-specific developmental timing is associated with differences in protein stability in mouse and human

Teresa Rayon[1*], Despina Stamataki[1#], Ruben Perez-Carrasco[1,2,3#], Lorena Garcia-Perez[1], Christopher Barrington[1], Manuela Melchionda[1], Katherine Exelby[1], Jorge Lazaro[1], Victor L. J. Tybulewicz [1,4], Elizabeth M. C. Fisher [5], James Briscoe [1*]

[1] The Francis Crick Institute, London, United Kingdom

[2] Department of Mathematics, University College London, London WC1E 6BT, UK

[3] Department of Life Sciences, Imperial College London, London SW7 2AZ, UK.

[4] Department of Immunology and Inflammation, Imperial College, London W12 0NN, UK

[5] UCL Queen Square Institute of Neurology, University College London, London WC1N 3BG, UK

[#]Equal contribution

*Correspondence to: james.briscoe@crick.ac.uk, teresa.rayon@crick.ac.uk

ABSTRACT

Although many molecular mechanisms controlling developmental processes are evolutionarily conserved, the speed at which the embryo develops can vary substantially between species. For example, the same genetic program, comprising sequential changes in transcriptional states, governs the differentiation of motor neurons in mouse and human, but the tempo at which it operates differs between species. Using in vitro directed differentiation of embryonic stem cells to motor neurons, we show that the program runs more than twice as fast in mouse as in human. This is not due to differences in signaling, nor the genomic sequence of genes or their regulatory elements. Instead, there is an approximately two-fold increase in protein stability and cell cycle duration in human cells compared to mouse. This can account for the slower pace of human development and suggests that differences in protein turnover play a role in interspecies differences in developmental tempo.

ONE SENTENCE SUMMARY

Comparison of mouse and human motor neuron differentiation suggests why developmental tempo differs between species.

MAIN TEXT

The events of embryonic development take place in a stereotypic sequence and at a characteristic tempo (*1*, *2*). Although the order and underlying molecular mechanisms are often indistinguishable between different species, the timescale and pace at which they progress can differ substantially. For example, compared to their rodent counterparts, neural progenitors in the primate cortex progress more slowly through a temporal sequence of neuronal subtype production (*3*, *4*). Moreover, the duration of cortical progenitor expansion differs between species of primates, at least partly accounting for differences in brain size (*5*, *6*). Even in more evolutionary conserved regions of the central nervous system (CNS) there are differences in tempo. The specification of neuronal subtype identity in the vertebrate spinal cord involves a well-defined gene regulatory program comprising a series of changes in transcriptional state as cells acquire specific identities as neural progenitors differentiate to post-mitotic neurons (*7*). The pace of this process differs between species, despite the similarity in the regulatory program and the structural and functional correspondence of the resulting spinal cords. The differentiation of motor neurons (MNs), a prominent neuronal subtype of the spinal cord, takes less than a day in zebrafish, 3-4 days in mouse, but ~2 weeks in human (*8*, *9*). Moreover, differences in developmental tempo are not confined to the CNS. The oscillatory gene expression that regulates the sequential formation of vertebrate body segments – the segmentation clock – has a

period that ranges from ~30mins in zebrafish, to 2-3h in mouse, and 5-6h in human (*10–12*). It is unclear as to what causes the interspecies differences in developmental tempo, termed developmental allochrony.

To address this question, we compared the generation of mouse and human MNs. Progenitors of the spinal cord initially express the transcription factors (TFs) Pax6 and Irx3 (*13*). Exposure to Sonic Hedgehog (Shh), emanating from the underlying notochord, results in ventrally located progenitors inducing Nkx6.1 and Olig2. This downregulates Pax6 and Irx3 (*14*). Progenitors expressing Olig2 and Nkx6.1 are termed pMNs and these either differentiate into post-mitotic MNs, which express a set of TFs including Hb9/Mnx1 and Isl1, or transition into p3 progenitors that express Nkx2.2 (*15*). This gene regulatory network (GRN), in which Olig2 represses Irx3 and Pax6 and promotes the differentiation of MNs, is conserved across vertebrates (*16*).

We used in vitro differentiation of MNs from mouse and human embryonic stem cells (ESCs) to investigate the pace of differentiation. We find that MN differentiation in vitro recapitulates species-specific global timescales observed in the embryos, lasting ~3 days in mouse and more than a week in human. We show that increased levels of signalling are unable to speed up the rate of differentiation of human cells. Moreover, by assaying the expression of a human gene, with its regulatory landscape, in a mouse context, we rule out the possibility that species differences in genomic sequence plays a major role in temporal scaling. Finally, we show that differences in protein degradation can explain the differences in developmental tempo.

RESULTS AND DISCUSSION

The characteristic spatial-temporal changes in gene expression and the regulatory interactions between the genes responsible for neural tube development are well described (*17*). Despite the conservation of the GRN across vertebrates, only limited analysis has been performed on the relevant stages of human development (*18*, *19*). We performed immunostainings on mouse and human embryonic spinal cords at brachial levels at equivalent stages (*20*) to more accurately correlate the major developmental events of neural differentiation processes in vivo between mouse and human (Fig. 1A). The dorsoventral (DV) length of the neural tube increases at the same rate in mouse and human (Fig S1A), and the shifts in gene expression are similar between mouse and human (Fig S1D). At their maximum extents, the OLIG2-expressing pMN domains comprise a large proportion of ventral progenitors, occupying approximately 30% of the DV length of the neural tube in mouse and a ~15% larger domain in human embryos (Fig. 1B, S1E). Consistent with this, there were more MN progenitors (pMN) in human but similar numbers of interneuron progenitors in mouse and human (Fig S1F). Over the following two days of mouse development, from E9.5 to E11.5, many post-mitotic MNs differentiate (Fig. 1C) resulting in a marked reduction in the size of the pMN domain (Fig. 1B), despite the continued proliferation of the progenitors (*9*). The proportion of neurons is higher in human compared to mouse (Fig S1B). By contrast, the pace of development is noticeably slower in human embryos. At Carnegie Stage (CS) 11 the pMN occupies a large proportion of the human neural tube, similar to the pMN in E9.0 mouse embryos. During the following 1-2 weeks of development (CS13-19, Fig. 1B), the size of the pMN decreases as MNs accumulate (Fig. 1C), but the rate of this change is slower than seen in mouse. MN production decreases at ~E11.5 in mouse whereas MN production continues to at least CS17 in human (Fig S1C), and glial progenitors, co-expressing SOX9 and NFIA, begin to arise in both species at these stages (Fig. 1D). Together, the data indicate an equivalent progression in neural tube development of mouse and human that lasts around 3 days in mouse and over a week in human (Fig. 1A).

We examined whether interspecies tempo differences were preserved in vitro. Methods for the differentiation of MNs from ESCs, which mimic in vivo developmental mechanisms, have been established for both mouse and human (*21–24*). To ensure comparison of similar axial levels in both species, we initially exposed mouse ESCs to a 20h pulse of WNT signalling, and human ESCs to a 72h pulse (*21*, *25*). This generated cells with a posterior epiblast identity – so called neuromesodermal progenitors – that express a suite of genes including T/TBXT, SOX2 and CDX2 (*21*, *26*) (Fig. S2A). These were then exposed to 100nM of Retinoic Acid (RA), which acts as a neuralizing signal, and to 500nM Smoothened agonist (SAG) that ventralises neural progenitors (*27*) (Fig. 2A,B). For both mouse and human, this resulted in the efficient generation of pMN expressing OLIG2 (Fig. 2C,D, S2B,C), and MNs expressing ISLET1 (ISL1), HB9/MNX1 and neuronal class III beta-tubulin (TUBB3) (Fig. 2E,F). Progenitors that had not differentiated into neurons switched from OLIG2 expressing pMN to p3 progenitors expressing NKX2.2 (Fig. 2C,D). Mouse and human

MNs expressed HOXC6, characteristic of forelimb level spinal cord MNs (*28*) (Fig. 2F), indicating pMN and MNs with similar axial levels were being produced in both cases.

Comparison of the two species revealed the same sequence of gene expression changes: expression of Pax6 in newly induced neural progenitors, followed by the expression of the pMN marker Olig2, which precedes the induction of post-mitotic MN markers, including Isl1 (Fig. 2C-G, S2B). But the rate of progression differed. Immunofluorescence and RT-qPCR assays for specific components of the GRN indicated that, after the addition of RA and SAG, the onset of ISL1 expression took 2-3 days in mouse, but ~6 days in human (Fig. 2E-G,K), consistent with the slower developmental progression in the developing human embryonic spinal cord. Moreover, Olig2 induction peaked after 2-3 days in mouse and 6-8 days in human (Fig. 2G, S2B). Differences in tempo have also been observed between the differentiation of mouse and human pluripotent stem cells (*29*). To test whether the difference in tempo of mouse and human MN differentiation represented a global change in the rate of developmental progression we performed bulk transcriptomics. This revealed a similar pattern of gene expression changes in mouse and human but the changes occurred at a faster rate in mouse cells than human cells (Fig. 2H). Cross-species comparison of dynamic genes highly expressed across the differentiation showed a high degree of correlation although altered in time between mouse and human (Fig. 2I, S2D). Moreover, the relative difference in developmental tempo appears constant throughout the differentiation process suggesting a global temporal scaling – developmental allochrony – between mouse and human.

To relate the tempo of mouse and human MN differentiation, we estimated the global difference in the tempo of gene expression comparing the Pearson correlation coefficients from the transcriptome analysis of both species. This identified a scaling factor of 2.5 ± 0.2 (median ± sd, Fig. 2I). Additionally, we clustered gene expression profiles into sets of genes with similar dynamics during the time course and we measured the fold difference in the time of appearance of the clusters that contained Pax6, Irx3, Olig2, Nkx2.2, Isl1 and Tubb3 genes. This confirmed that a scaling factor of ~2.5 fit each of the gene expression clusters (Fig. 2J). Similarly, time factor measurements for individual genes identified a scaling factor between 2-3 (Fig. S2F,G). To test if the identified time factor could be extended to the whole transcriptome, we selected four cluster pairs comprising a high proportion of orthologous genes (Fig. S2E). A search for a scaling factor that accommodated the difference in the timing of expression in these groups indicated a factor of ~2.5 for each of the clusters (Fig. 2L). Together, these results suggest that MN differentiation can be recapitulated in vitro from mouse and human ESCs and results in a global 2.5- fold decrease in the rate at which gene expression programs advance in human compared to mouse.

Sonic Hedgehog Signalling Sensitivity Does Not Regulate Tempo

Having identified a global scaling factor for the GRN, we investigated the mechanism that sets the timescale. We reasoned that the mechanism was likely to be cell-autonomous since the temporal differences are observed between mouse and human cells grown in vitro, and it has been shown that in vitro differentiated cells transplanted to a host follow their own species-specific dynamics (*30–32*). Since the directed differentiation towards MNs occurs in response to Shh signalling, we hypothesized that the delay in the GRN in human compared to mouse could be a consequence of a reduced sensitivity to signalling. To test whether the human GRN could be sped up by higher levels of signalling, we differentiated human progenitors in the presence of increasing concentrations of SAG and in a combination of SAG and Purmorphamine (Pur), another smoothened agonist (Fig. 3A). Single cell measurements of NKX6.1, a GRN transcription factor induced by Shh in ventral progenitors, showed similar proportions and intensity of expression for all levels of signal at equivalent time-points (Fig. S3A,B). To test whether the competence of neural progenitors to respond to Shh was delayed in human compared to mouse, we delayed addition of SAG for 24h. A 24h delay in Shh addition resulted in higher initial levels of *IRX3*, as expected, but did not change the time of *NKX6.1, GLI1 or PTCH1* induction relative to the time of SAG addition (Fig. 3C, S3D), corroborating that the onset of Shh responsiveness is acquired at neural induction in human as in mouse cells.

We then compared the kinetics of Shh signalling in mouse and human cells by assaying the response of Ptch1 and Gli1, two Shh pathway components that are Shh direct target genes (*33*, *34*). Strikingly, the response dynamics of these two genes were similar in mouse and human. In both species, the expression levels of Ptch1 and Gli1 were increased within 12h and peaked by 24h (Fig. 3D,S3E). By contrast, the induction of Nkx6.1 was delayed 48h in human compared to mouse (Fig. 3D). Additional components of the Shh signaling pathway, including Gli2, Ptch2 and Hhip,

also showed increased expression within 24h (Fig. S3F). The induction of Olig2, similarly to Nkx6.1, was delayed in human compared to mouse (Fig. S3F). Together, these results suggest that differential sensitivity to extrinsic signals does not appear to have a major role in regulating the tempo of development.

No Effect of Interspecies Sequence Differences in Gene Regulation

Having ruled out a role for Shh signalling, we focused on possible interspecies sequence differences in gene regulation. Even though genes in the GRN are highly conserved compared to the average identity between human and mouse (Supp Data S1), we hypothesized that sequence differences in the coding region and/or cis-regulatory elements might determine the pace of development. To study sequence differences between species, we focused on Olig2 because it is the major regulator of pMN identity and its cis-regulatory elements have been characterized (*35*, *36*). We reasoned that if sequence differences were responsible for the different temporal dynamics in mouse and human cells, we would be able to detect species-specific changes in the timing of Olig2 expression from a human Olig2 locus introduced into mouse cells. The human Olig2 gene is located on chromosome 21, and we took advantage of the 47-1 mouse ESC line that contains the Hsa21q arm of human chromosome 21 (*37*). We differentiated the 47-1 line (hereafter referred to as hChr21) alongside its parental line, which lacked Hsa21q, from which it was generated (hereafter referred to as wt). The proportions of neural progenitors and the dynamics of gene expression, measured by RNA expression, immunofluorescence and flow cytometry, were similar between hChr21 and wt lines (Fig. 4A,B S4A,B). We then assessed the timing of expression of the *hOLIG2* allele. We detected induction of *hOLIG2* at Day 1 of differentiation (Fig. 4B), 24h after addition of RA and SAG. By contrast in human cells, *hOLIG2* induction is not detected until Day 2-3 (Fig. 2G). Thus, in mouse cells, *hOLIG2* follows the same dynamics of gene expression as mouse *Olig2* (*mOlig2*), indicating that the temporal control of gene expression depends on the cellular environment and not the species origin of the genomic sequence.

To compare Olig2 expression levels between the mouse and human alleles, we performed single-molecule Fluorescent In Situ Hybridization (smFISH) (Fig. 4C,D, S5A,B). We first assayed transcripts of *Sox2* (*mSox2*), a transcription factor expressed in all neural progenitors. The mean and variance in *mSox2* transcripts were similar in both hChr21 and wt neural progenitors, supporting the comparability of the two cell lines (Fig. S5C). We then measured Olig2 transcripts using species-specific probes. The number of mouse Olig2 (*mOlig2*) transcripts in hChr21 cells was lower than in wt cells, but the mean total number of Olig2 transcripts in hChr21 cells, combining mouse and human alleles, was higher than the mean number of transcripts in wt cells (Fig. 4E). This suggests that the number of transcripts that cells express depends on the number of the alleles.

We next asked whether the levels of specific mRNAs were similar in human cells to those in mouse. To this end, we performed smFISH in human neural progenitors for *SOX2* (*hSOX2*) and *OLIG2* (*hOLIG2*) (Fig. 4D, S5B). The median number of *hOLIG2* molecules in human cells at days 4, 6 and 8 was similar, indicating that the number of transcripts is constant in cells (Fig. S5E). The number of Sox2 and Olig2 transcripts in human neural progenitors were higher than in mouse wt (Fig. S5C). However, human neural progenitors were larger than mouse progenitors (Fig. S5D) and taking this into account allowed calculation of the concentration of RNAs (mRNAs/μm^2) in human and mouse cells (Fig. 4F). The mean concentration of total Olig2 in mouse hChr21 cells was more similar to the concentration of *mOlig2* in wt mouse cells than the concentration of *hOLIG2* in human cells (mean difference of 0.121 mRNAs/μm^2 (95% CI: [0.101; 0.141]) between mouse and hChr21 cells; with a mean difference of 0.157 mRNAs/μm^2 (95% CI: [0.139; 0.175]) between human and hChr21 cells) (Fig. 4F), indicating that mRNA concentration might be controlled by the cellular context. Overall, we conclude that gene regulation in mouse cells follows mouse-specific characteristics, irrespective of the species origin of the allele, suggesting that species differences in gene expression dynamics are not encoded within the regulatory genome of individual genes.

Kinetics of the Proteome Correspond with The Interspecies Dynamics of Differentiation

Given that the species difference in tempo did not appear to depend on species-specific differences in genomic elements, we reasoned that kinetic features of gene expression must explain the difference, similar to the findings in synthetic biology and modeling fields (*38*, *39*). We therefore set out to measure the decay rate of transcripts and proteins in mouse and human neural progenitors, which encompasses both degradative mechanisms and dilution

from cell division (*40*). To assay mRNA decay, we used the uridine analogue, 5-ethynyluridine (EU) and assayed mouse neural progenitors from Day 2 and human neural progenitors from Day 4 and 8, representing equivalent developmental states in the two species (Fig. S2C). We pulsed cells for 3h to label actively transcribing mRNAs, transferred them to media lacking EU and assayed the EU remaining in cells at regular timepoints (Fig S6A,B). FACS analysis suggested a similar global mRNA stability in mouse and human neural progenitors, with a median half-life ($t_{1/2}$) of 92 ± 33.3 min in mouse cells and a $t_{1/2}$ of 76 ± 19.7 min in human Day 4 and 96 ± 37.6 min at Day 8 (Fig. 5A,B). This agrees with measurements of mRNA half-lives in other cell lines (*41*). Consistent with this, measuring the stability of selected individual mRNAs also suggested similar half-life of mRNAs in mouse and human neural progenitors (Fig. S6E). Nevertheless, extending and refining these measurements will provide insight into whether there are detectable differences in mRNA stability between species and how these contribute to the cellular concentrations of specific transcripts (*12*).

Next, we tested whether differences in protein decay rate could explain the allochrony. To assay protein stability, we metabolically labelled nascent proteins replacing methionine in the medium with the methionine analog L-azidohomoalanine (AHA), and used FACS to measure the stability of newly synthesized proteins upon removal of the amino acid analog over the course of 48h (Fig S6C,D). We found that the half-life of the proteome in mouse neural progenitors was shorter than in human progenitors ($t_{1/2}$ = 7.8h ± 1.6h in mouse versus $t_{1/2}$ = 19.3h ± 5.2h in human Day 4 or $t_{1/2}$ = 18.2h ± 2.3h in human Day 8), corresponding to a 2-2.5- fold difference (Fig. 5C,D). This identifies a general difference in the protein lifetime between mouse and human that corresponds to the difference in tempo, and further analysis will be required to determine which specific proteins show a 2-2.5- fold difference.

To test whether changes in mRNA or protein stability could account for differences in developmental tempo, we developed a computational model of the GRN based on a previous model describing the dynamics of the mouse neural progenitor GRN (Fig. 5E) (*42*). The model incorporates separately the dynamics of mRNA and protein (see Supplementary text). Simulations showed a good correspondence with the temporal dynamics measured in mouse cells (Fig. 5E, Fig. 2G). Halving the decay rate of the proteins (but not mRNA) to mimic the measured human kinetics, resulted in the same sequence of gene expression but slower dynamics of the GRN (Fig. 5E). To explore further the connection between changes in protein stability and GRN dynamics, we measured the change in time of the onset of Olig2 (we refer to this as the time factor) for different values of mRNA and protein stability. This revealed that increasing mRNA stability had less effect than increasing protein stability on the time factor. In particular, the model predicted that, if protein decay was kept constant, a 4- fold change in mRNA stability would be required to reproduce the observed temporal scaling of 2.5 in human versus mouse (Fig. 5F). Such a fold change in mRNA stability is not compatible with our global measurements (Fig. 5B), suggesting that differences in mRNA kinetics between species might be less influential given the timescales of MN differentiation. Moreover, the relationship between the tempo scaling observed in the simulations with the changes in protein decay rate revealed a superlinear relationship in which an increase in protein stability slowed GRN dynamics by slightly more than the fold increase in decay rate (Fig. 5G, S7C). These results indicated that the measured increase in protein stability can explain tempo changes in MN differentiation between mouse and human.

To explore whether other aspects of gene regulation might contribute to differences in tempo, we undertook a computational screen in which decay and production rates of mRNA and protein were allowed to change independently. In addition, the TF binding affinities of the model were also allowed to vary within previously defined constraints (*42*). We identified parameter sets that reproduced the ~2.5- fold difference in tempo (Fig. S7A,B). The resulting ensemble of parameters showed a wide range of transcription and translation rates for which the network reproduces the tempo differences between human and mouse (Fig. S7A, B). There were no apparent changes in the constraints on the parameters of the model, with the exception of the protein decay rate, which showed a narrow distribution centered around a 2.5- fold change (Fig. S7A). These results indicate that control of protein decay rate is an effective mechanism to regulate developmental tempo.

A prediction that arises from this analysis is that the TFs comprising the GRN that regulate MN differentiation should be more stable in human than in mouse neural progenitors, and that a 2- fold decrease in protein decay would give a scaling factor of ~2.5. To test this, we performed pulse-chase experiments labeling nascent proteins with AHA, conjugated labelled proteins to biotin, and pulled them down with streptavidin beads to purify. This revealed that pan-neural proteins SOX1 and SOX2 had longer lifetimes than OLIG2 and NKX6.1 proteins in both species (Fig. 6A,

S6F,G). Moreover, human NKX6.1 and OLIG2 were ~2- fold more stable than their mouse homologues (mNKX6.1 ≈ 2.5h vs. hNKX6.1 ≈ 6h; mOLIG2 ≈ 3.5h, hOLIG2 ≈ 6.8h) (Fig. 6A, S6F,G). These results are consistent with the predictions of the model and the non-linear relationship between decay rates and tempo scaling.

The identification of a global increase in the lifetime of proteins in human compared to mouse neural progenitors raised the possibility that exogenous proteins would show species-specific stability. To this end, we generated Patched1::mKate2 reporter lines in mouse and human stem cells. In these lines, the monomeric far-red fluorescent protein Katushka-2 (mKate2) was fused to the C-terminus of endogenous Ptch1 via a self-cleaving peptide (Fig. S8A). This way, we could modulate mKATE2 expression, driven by the Shh responsive Ptch1, using small molecule activators and inhibitors of Shh signalling. To measure mKATE2 stability in neural progenitors, we induced mKate2 expression by addition of SAG (Fig. S8B). Then we added the Smoothened antagonist Vismodegib (*43*) to block Shh signalling thereby repressing new mKATE2 production. We assayed the decay of mKATE2 fluorescence in inhibited cells. FACS analysis showed a half-life of 17.7h ± 2.3h for mKate2 in mouse cells. By contrast, the half-life of the same mKATE2 protein in human cells was 32.9h ± 7.3h (Fig 6B,C). These results indicate that protein half-life is species-specific.

The long half-life of mKATE2 raised the possibility that dilution, following cell division, contributed to the measured decay rate (*40*). Differences in the cell cycle time between mouse and human cells have been measured (*44–47*), and could therefore contribute to the difference in mKATE2 lifetime in neural progenitors. To test this, we assayed total cell cycle length using cumulative EdU labelling of mouse and human neural progenitors (Fig. 6D, E, S9A,B) (*48*). Cell cycle duration in equivalent staged neural progenitors from mouse and human was 10.8h ± 8.3h compared to 28.4h ± 13.9h, respectively in accordance with cell cycle measurements in other human and mouse cell types (*44–47*). Thus, similar to the proteome, the cell cycle operates 2-2.5 times faster in mouse compared to human. Since progress through the cell cycle is controlled by protein degradation (*49, 50*), the difference in cell cycle rate between mouse and human cells may also be a consequence of a global change in protein stability.

Taken together, the data indicate that the dynamics of the GRN associated with the embryonic generation of MNs progresses 2-3 times faster in mouse than in human cells. A similar difference in the tempo of the segmentation clock between mouse and human has also been observed (*10, 12*). These differences do not appear to arise from a bottleneck caused by a specific rate limiting event in MN generation. Moreover, neither changes in the dynamics of signalling nor variations in genomic regulatory sequences appear to account for the species-specific tempos. Instead, the correlated ~2.5- fold differences in cell cycle length and general protein stability suggest that the temporal scaling in developmental processes results from global differences in key kinetic parameters that broadly affect the tempo of molecular processes. What sets this global tempo remains to be determined but could involve the differences in the rates of pivotal molecular processes such as global changes in proteostasis or differences in the overall metabolic rate of cells. How these affect the pace at which GRNs elaborate and how such variations are assimilated to ensure the development of robust and appropriately proportioned tissues need to be addressed. The availability of in vitro systems that mimic in vivo developmental allochrony open up the possibility of exploring these issues.

REFERENCES

1. K. Toma, T.-C. Wang, C. Hanashima, Encoding and decoding time in neural development. *Development, Growth & Differentiation*. **58**, 59–72 (2016).

2. M. Ebisuya, J. Briscoe, What does time mean in development? *Development (Cambridge, England)*. **145**, dev164368 (2018).

3. S. Herculano-Houzel, The remarkable, yet not extraordinary, human brain as a scaled-up primate brain and its associated cost. *Proceedings of the National Academy of Sciences of the United States of America*. **109 Suppl 1**, 10661–8 (2012).

4. J. van den Ameele, L. Tiberi, P. Vanderhaeghen, I. Espuny-Camacho, Thinking out of the dish: what to learn about cortical development using pluripotent stem cells. *Trends in Neurosciences*. **37**, 334–342 (2014).

5. C. C. Gertz, J. H. Lui, B. E. LaMonica, X. Wang, A. R. Kriegstein, Diverse behaviors of outer radial glia in developing ferret and human cortex. *The Journal of neuroscience : the official journal of the Society for Neuroscience*. **34**, 2559–70 (2014).

6. D. V. Hansen, J. H. Lui, P. R. L. Parker, A. R. Kriegstein, Neurogenic radial glia in the outer subventricular zone of human neocortex. *Nature*. **464**, 554–561 (2010).

7. J. Briscoe, S. Small, Morphogen rules: design principles of gradient-mediated embryo patterning. *Development (Cambridge, England)*. **142**, 3996–4009 (2015).

8. B. N. Davis-Dusenbery, L. A. Williams, J. R. Klim, K. C. Eggan, How to make spinal motor neurons. *Development*. **141**, 491–501 (2014).

9. A. Kicheva, T. Bollenbach, A. Ribeiro, H. P. Valle, R. Lovell-Badge, V. Episkopou, J. Briscoe, Coordination of progenitor specification and growth in mouse and chick spinal cord. *Science (New York, N.Y.)*. **345**, 1254927 (2014).

10. C. Gomez, E. M. Özbudak, J. Wunderlich, D. Baumann, J. Lewis, O. Pourquié, Control of segment number in vertebrate embryos. *Nature*. **454**, 335–339 (2008).

11. A. Hubaud, O. Pourquié, Signalling dynamics in vertebrate segmentation. *Nature Reviews Molecular Cell Biology*. **15** (2014), pp. 709–721.

12. M. Matsuda, H. Hayashi, J. Garcia-Ojalvo, K. Yoshioka-, R. Kageyama, Y. Yamanaka, M. Ikeya, C. Alev, M. Ebisuya, Species-specific oscillation periods of human and mouse segmentation clocks, doi:10.1101/650648.

13. J. Briscoe, A. Pierani, T. M. Jessell, J. Ericson, A homeodomain protein code specifies progenitor cell identity and neuronal fate in the ventral neural tube. *Cell*. **101**, 435–445 (2000).

14. E. Dessaud, A. P. McMahon, J. Briscoe, Pattern formation in the vertebrate neural tube: a sonic hedgehog morphogen-regulated transcriptional network. *Development*. **135**, 2489–2503 (2008).

15. E. Dessaud, L. L. Yang, K. Hill, B. Cox, F. Ulloa, A. Ribeiro, A. Mynett, B. G. Novitch, J. Briscoe, Interpretation of the sonic hedgehog morphogen gradient by a temporal adaptation mechanism. *Nature*. **450**, 717–720 (2007).

16. C. Catela, P. Kratsios, Transcriptional mechanisms of motor neuron development in vertebrates and invertebrates. *Developmental Biology* (2019), doi:10.1016/J.YDBIO.2019.08.022.

17. J. Briscoe, S. Small, Morphogen rules: design principles of gradient-mediated embryo patterning.

Development. **142**, 3996–4009 (2015).

18. U. Marklund, E. M. Hansson, E. Sundstrom, M. H. de Angelis, G. K. H. Przemeck, U. Lendahl, J. Muhr, J. Ericson, Domain-specific control of neurogenesis achieved through patterned regulation of Notch ligand expression. *Development*. **137**, 437–445 (2010).

19. M. W. Amoroso, G. F. Croft, D. J. Williams, S. O 'keeffe, M. A. Carrasco, A. R. Davis, L. Roybon, D. H. Oakley, T. Maniatis, C. E. Henderson, H. Wichterle, Cellular/Molecular Accelerated High-Yield Generation of Limb-Innervating Motor Neurons from Human Stem Cells, doi:10.1523/JNEUROSCI.0906-12.2013.

20. J. Kerwin, Y. Yang, P. Merchan, S. Sarma, J. Thompson, X. Wang, J. Sandoval, L. Puelles, R. Baldock, S. Lindsay, The HUDSEN Atlas: a three-dimensional (3D) spatial framework for studying gene expression in the developing human brain. *Journal of anatomy*. **217**, 289–99 (2010).

21. M. Gouti, A. Tsakiridis, F. J. Wymeersch, Y. Huang, J. Kleinjung, V. Wilson, J. Briscoe, In vitro generation of neuromesodermal progenitors reveals distinct roles for wnt signalling in the specification of spinal cord and paraxial mesoderm identity. *PLoS biology*. **12**, e1001937 (2014).

22. S. M. Chambers, C. A. Fasano, E. P. Papapetrou, M. Tomishima, M. Sadelain, L. Studer, Highly efficient neural conversion of human ES and iPS cells by dual inhibition of SMAD signaling. *Nature Biotechnology*. **27**, 275–280 (2009).

23. H. Lee, G. Al Shamy, Y. Elkabetz, C. M. Schofield, N. L. Harrsion, G. Panagiotakos, N. D. Socci, V. Tabar, L. Studer, Directed Differentiation and Transplantation of Human Embryonic Stem Cell-Derived Motoneurons. *Stem Cells*. **25**, 1931–1939 (2007).

24. R. Patani, A. J. Hollins, T. M. Wishart, C. A. Puddifoot, S. Álvarez, A. R. de Lera, D. J. A. Wyllie, D. A. S. Compston, R. A. Pedersen, T. H. Gillingwater, G. E. Hardingham, N. D. Allen, S. Chandran, Retinoid-independent motor neurogenesis from human embryonic stem cells reveals a medial columnar ground state. *Nature Communications*. **2**, 214 (2011).

25. E. S. Lippmann, C. E.williams, D. A. Ruhl, M. C. Estevez-Silva, E. R. Chapman, J. J. Coon, R. S. Ashton, Deterministic HOX patterning in human pluripotent stem cell-derived neuroectoderm. *Stem Cell Reports*. **4**, 632–644 (2015).

26. V. Metzis, S. Steinhauser, E. Pakanavicius, M. Gouti, D. Stamataki, K. Ivanovitch, T. Watson, T. Rayon, S. N. Mousavy Gharavy, R. Lovell-Badge, N. M. Luscombe, J. Briscoe, Nervous System Regionalization Entails Axial Allocation before Neural Differentiation. *Cell*. **175**, 1105-1118.e17 (2018).

27. A. Sagner, Z. B. Gaber, J. Delile, J. H. Kong, D. L. Rousso, C. A. Pearson, S. E. Weicksel, M. Melchionda, S. N. Mousavy Gharavy, J. Briscoe, B. G. Novitch, Olig2 and Hes regulatory dynamics during motor neuron differentiation revealed by single cell transcriptomics. *PLOS Biology*. **16**, e2003127 (2018).

28. J. S. Dasen, J.-P. Liu, T. M. Jessell, Motor neuron columnar fate imposed by sequential phases of Hox-c activity. *Nature*. **425**, 926–933 (2003).

29. C. Barry, M. T. Schmitz, C. Argus, J. M. Bolin, M. D. Probasco, N. Leng, B. M. Duffin, J. Steill, S. Swanson, B. E. McIntosh, R. Stewart, C. Kendziorski, J. A. Thomson, R. Bacher, Automated minute scale RNA-seq of pluripotent stem cell differentiation reveals early divergence of human and mouse gene expression kinetics. *PLOS Computational Biology*. **15**, e1007543 (2019).

30. C. Barry, M. T. Schmitz, P. Jiang, M. P. Schwartz, B. M. Duffin, S. Swanson, R. Bacher, J. M. Bolin, A. L. Elwell, B. E. McIntosh, R. Stewart, J. A. Thomson, Species-specific developmental timing is maintained by pluripotent stem cells ex utero. *Developmental Biology*. **423**, 101–110 (2017).

31.   N. Gaspard, T. Bouschet, R. Hourez, J. Dimidschstein, G. Naeije, J. van den Ameele, I. Espuny-Camacho, A. Herpoel, L. Passante, S. N. Schiffmann, A. Gaillard, P. Vanderhaeghen, An intrinsic mechanism of corticogenesis from embryonic stem cells. *Nature*. **455**, 351–357 (2008).

32.   D. Linaro, B. Vermaercke, R. Iwata, A. Ramaswamy, B. Libé-Philippot, L. Boubakar, B. A. Davis, K. Wierda, K. Davie, S. Poovathingal, P.-A. Penttila, A. Bilheu, L. De Bruyne, D. Gall, K.-K. Conzelmann, V. Bonin, P. Vanderhaeghen, Xenotransplanted Human Cortical Neurons Reveal Species-Specific Development and Functional Integration into Mouse Visual Circuits. *Neuron*. **104**, 972-986.e6 (2019).

33.   J. Lee, K. A. Platt, P. Censullo, A. Ruiz i Altaba, Gli1 is a target of Sonic hedgehog that induces ventral neural tube development. *Development*. **124** (1997).

34.   V. Marigo, C. J. Tabin, Regulation of patched by sonic hedgehog in the developing neural tube. *Proceedings of the National Academy of Sciences of the United States of America*. **93**, 9346–9351 (1996).

35.   T. Oosterveen, S. Kurdija, Z. Alekseenko, C. W. Uhde, M. Bergsland, M. Sandberg, E. Andersson, J. M. Dias, J. Muhr, J. Ericson, Mechanistic Differences in the Transcriptional Interpretation of Local and Long-Range Shh Morphogen Signaling. *Developmental Cell*. **23**, 1006–1019 (2012).

36.   K. a. Peterson, Y. Nishi, W. Ma, A. Vedenko, L. Shokri, X. Zhang, M. McFarlane, J.-M. M. Baizabal, J. P. Junker, A. van Oudenaarden, T. Mikkelsen, B. E. Bernstein, T. L. Bailey, M. L. Bulyk, W. H. Wong, A. P. McMahon, Neural-specific Sox2 input and differential Gli-binding affinity provide context and positional information in Shh-directed neural patterning. *Genes and Development*. **26**, 2802–2816 (2012).

37.   D. Hernandez, P. J. Mee, J. E. Martin, V. L. J. Tybulewicz, E. M. C. Fisher, Transchromosomal mouse embryonic stem cell lines and chimeric mice that contain freely segregating segments of human chromosome 21. *Human molecular genetics*. **8**, 923–33 (1999).

38.   F. Cacace, P. Paci, V. Cusimano, A. Germani, L. Farina, Stochastic Modeling of Expression Kinetics Identifies Messenger Half-Lives and Reveals Sequential Waves of Co-ordinated Transcription and Decay. *PLoS Computational Biology*. **8**, e1002772 (2012).

39.   N. Rosenfeld, U. Alon, Response delays and the structure of transcription networks. *J Mol Biol*. **329**, 645–654 (2003).

40.   E. Eden, N. Geva-Zatorsky, I. Issaeva, A. Cohen, E. Dekel, T. Danon, L. Cohen, A. Mayo, U. Alon, Proteome Half-Life Dynamics in Living Human Cells. *Science*. **331**, 764–768 (2011).

41.   C. C. Friedel, L. Dölken, Z. Ruzsics, U. H. Koszinowski, R. Zimmer, Conserved principles of mammalian transcriptional regulation revealed by RNA half-life. *Nucleic acids research*. **37**, e115 (2009).

42.   M. Cohen, K. M. Page, R. Perez-Carrasco, C. P. Barnes, J. Briscoe, A theoretical framework for the regulation of Shh morphogen-controlled gene expression. *Development*. **141**, 3868–3878 (2014).

43.   C. M. Rudin, C. L. Hann, J. Laterra, R. L. Yauch, C. A. Callahan, L. Fu, T. Holcomb, J. Stinson, S. E. Gould, B. Coleman, P. M. LoRusso, D. D. Von Hoff, F. J. de Sauvage, J. A. Low, Treatment of Medulloblastoma with Hedgehog Pathway Inhibitor GDC-0449. *New England Journal of Medicine*. **361**, 1173–1178 (2009).

44.   D. R. Kornack, P. Rakic, Changes in cell-cycle kinetics during the development and evolution of primate neocortex. *Proceedings of the National Academy of Sciences of the United States of America*. **95**, 1242–1246 (1998).

45.   N. A. J. Krentz, D. van Hoof, Z. Li, A. Watanabe, M. Tang, C. Nian, M. S. German, F. C. Lynn, Phosphorylation of NEUROG3 Links Endocrine Differentiation to the Cell Cycle in Pancreatic Progenitors. *Developmental*

Cell. **41**, 129-142.e6 (2017).

46.   F. Mora-Bermudez, F. Badsha, S. Kanton, J. G. Camp, B. Vernot, K. K?hler, B. Voigt, K. Okita, T. Maricic, Z. He, R. Lachmann, S. P??bo, B. Treutlein, W. B. Huttner, A. Musacchio, Differences and similarities between human and chimpanzee neural progenitors during cerebral cortex development. *eLife*. **5**, 371–5 (2016).

47.   T. Otani, M. C. C. Marchetto, F. H. H. Gage, B. D. D. Simons, F. J. J. Livesey, 2D and 3D Stem Cell Models of Primate Cortical Development Identify Species-Specific Differences in Progenitor Behavior Contributing to Brain Size. *Cell Stem Cell*. **18**, 467–480 (2016).

48.   R. S. Nowakowski, S. B. Lewin, M. W. Miller, Bromodeoxyuridine immunohistochemical determination of the lengths of the cell cycle and the DNA-synthetic phase for an anatomically defined population. *Journal of Neurocytology*. **18**, 311–318 (1989).

49.   R. W. King, R. J. Deshaies, J.-M. Peters, M. W. Kirschner, How Proteolysis Drives the Cell Cycle. *Science*. **274**, 1652–1659 (1996).

50.   D. M. Koepp, *Cell Cycle Regulation by Protein Degradation* (2014; http://link.springer.com/10.1007/978-1-4939-0888-2_4).

51.   N. Balaskas, A. Ribeiro, J. Panovska, E. Dessaud, N. Sasai, K. M. Page, J. Briscoe, V. Ribes, Gene regulatory logic for reading the sonic hedgehog signaling gradient in the vertebrate neural tube. *Cell*. **148**, 273–284 (2012).

52.   M. Zagorski, A. Kicheva, in *Methods in Molecular Biology* (Humana Press Inc., 2018), vol. 1863, pp. 47–63.

53.   M. Gouti, J. Delile, D. Stamataki, F. J. Wymeersch, Y. Huang, J. Kleinjung, V. Wilson, J. Briscoe, A Gene Regulatory Network Balances Neural and Mesoderm Specification during Vertebrate Trunk Development. *Developmental Cell*. **41**, 243--261.e7 (2017).

54.   P. Di Tommaso, M. Chatzou, E. W. Floden, P. P. Barja, E. Palumbo, C. Notredame, Nextflow enables reproducible computational workflows. *Nature Biotechnology*. **35**, 316–319 (2017).

55.   B. L. Aken, P. Achuthan, W. Akanni, M. R. Amode, F. Bernsdorff, J. Bhai, K. Billis, D. Carvalho-Silva, C. Cummins, P. Clapham, L. Gil, C. G. Girón, L. Gordon, T. Hourlier, S. E. Hunt, S. H. Janacek, T. Juettemann, S. Keenan, M. R. Laird, I. Lavidas, T. Maurel, W. McLaren, B. Moore, D. N. Murphy, R. Nag, V. Newman, M. Nuhn, C. K. Ong, A. Parker, M. Patricio, H. S. Riat, D. Sheppard, H. Sparrow, K. Taylor, A. Thormann, A. Vullo, B. Walts, S. P. Wilder, A. Zadissa, M. Kostadima, F. J. Martin, M. Muffato, E. Perry, M. Ruffier, D. M. Staines, S. J. Trevanion, F. Cunningham, A. Yates, D. R. Zerbino, P. Flicek, Ensembl 2017. *Nucleic Acids Research*. **45**, D635–D642 (2017).

56.   L. Wang, S. Wang, W. Li, RSeQC: quality control of RNA-seq experiments. *Bioinformatics*. **28**, 2184–2185 (2012).

57.   D. S. DeLuca, J. Z. Levin, A. Sivachenko, T. Fennell, M.-D. Nazaire, C. Williams, M. Reich, W. Winckler, G. Getz, RNA-SeQC: RNA-seq metrics for quality control and process optimization. *Bioinformatics*. **28**, 1530–1532 (2012).

58.   A. Dobin, C. A. Davis, F. Schlesinger, J. Drenkow, C. Zaleski, S. Jha, P. Batut, M. Chaisson, T. R. Gingeras, STAR: ultrafast universal RNA-seq aligner. *Bioinformatics*. **29**, 15–21 (2013).

59.   B. Li, C. N. Dewey, RSEM: accurate transcript quantification from RNA-Seq data with or without a reference genome. *BMC Bioinformatics*. **12**, 323 (2011).

60.   I. C. McDowell, D. Manandhar, C. M. Vockley, A. K. Schmid, T. E. Reddy, B. E. Engelhardt, Clustering gene

expression time series data using an infinite Gaussian process mixture model. *PLOS Computational Biology*. **14**, e1005896 (2018).

61. G. C. and T. Nepusz, The igraph software package for complex network research. *InterJournal*. **Complex Sy**, 1695 (2006).

62. F. De Chaumont, S. Dallongeville, N. Chenouard, N. Hervé, S. Pop, T. Provoost, V. Meas-Yedid, P. Pankajakshan, T. Lecomte, Y. Le Montagner, T. Lagache, A. Dufour, J. C. Olivo-Marin, Icy: An open bioimage informatics platform for extended reproducible research. *Nature Methods*. **9**, 690–696 (2012).

63. E. M. Shockley, J. A. Vrugt, C. F. Lopez, PyDREAM: high-dimensional parameter inference for biological models in python. *Bioinformatics*. **34**, 695–697 (2018).

64. E. Laloy, J. A. Vrugt, High-dimensional posterior exploration of hydrologic models using multiple-try DREAM (ZS) and high-performance computing. *Water Resources Research*. **48** (2012), doi:10.1029/2011WR010608.

AUTHOR CONTRIBUTIONS

T.R. and J.B. conceived the project, interpreted the data, and wrote the manuscript with input from all authors. T.R. designed and performed experiments and data analysis. D.S. designed and performed experiments and data analysis. R.P.C. performed theoretical modelling and data analysis. L.G.P. designed experiments and performed data analysis for smFISH. C.B. performed bioinformatic analysis. M.M. performed embryo work, generated and characterized the Ptch1::T2A-mKate2 mouse ES cell line. K.E. performed embryo work. J.L. analysed embryo data. E.M. and V.T. provided reagents and feedback.

COMPETING INTERESTS

The authors declare no competing or financial interests.

DATA AND MATERIALS AVAILABILITY

The accession number for the bulk RNA-seq data reported in this paper is GSE140749.

SUPPLEMENTARY MATERIALS
Materials and Methods
Supplementary Text
Fig. S1 - S8
Table S1 - S2
Data S1

FIGURE LEGENDS

Figure 1. Comparison of neural tube development in mouse and human embryos.

(**A**) Schema of mouse and human neural tube development (**B-D**). Immunofluorescence in transverse sections of mouse and human cervical neural tube from E9.0 to E11.5 in mouse and CS11 to CS17 in human embryos. (**B**) Expression of progenitor markers PAX6 (green), OLIG2 (magenta) and NKX2.2 (cyan). (**C**) Pan-neural progenitor marker SOX2 (blue), motor neuron markers ISL1 (magenta) and HB9/MNX1 (cyan) at neurogenic stages. (**D**) Ventral expression of gliogenic markers NFIA (red) and SOX9 (blue) in the neural tube can be detected from E10.5 in mouse and CS15 in human. NFIA also labels neurons, as indicated by TUBB3 (cyan) staining. Scale bars = 50 microns.

Figure 2. A global scaling factor for in vitro differentiation of mouse and human MNs.

(**A**) Schema of mouse ESCs differentiated to MNs. Spinal cord progenitors generated via an NMP state induced by the addition of FGF, WNT and dual SMAD inhibition signals for 24h (blue rectangle), subsequently exposed to the neuralizing signal retinoic acid (RA) and smoothened agonist (SAG) to ventralise the cells (green). (**B**) Schema of the analogous strategy used for human ESCs to generate MNs, where the addition of FGF, WNT and dual SMAD inhibition signals lasts 72h. (**C**) Expression of NP markers (PAX6, OLIG2, NKX2.2) between Days 1 and 3 in mouse MN differentiation. (**D**) Expression of NP markers (PAX6, OLIG2, NKX2.2) at Days 4, 6 and 8 in human MN differentiation. (**E**) Expression of MN markers (ISL1, HB9/MNX1) in mouse and human MNs. Mouse MNs can be detected by Days 2-3, whereas human MNs are not detected until Days 8 and 10. (**F**) HOXC6 expression in MNs characterized by ISL1 and TUBB3 expression at Day 3 in mouse and in human Day 10. Scale bars = 50 microns. (**G**) RT-qPCR analysis of Pax6, Olig2, Nkx2.2 and Isl1 expression in mouse and human differentiation reveals a conserved progression in gene expression but a different tempo (human n = 3 in triplicate, mouse n = 3 in triplicate). (**H**) Heatmap of RNA-seq data from mouse and human MN differentiation indicating the normalized expression of selected markers representative of neuromesodermal progenitors, neural progenitors, neurons, glia and mesoderm cell types (mouse n = 3, human n = 3). (**I**) Heatmap of the pair wise Pearson correlation coefficients of the transcriptomes of mouse (vertical) and human (horizontal) differentiation at the indicated time points. High positive correlation indicated by values close to 1 (red). White line shows a linear fit of the Pearson correlation with temporal scaling factor of 2.5 ± 0.2 (median ± std). (**J**) Scaling factor for transcriptome clusters that contain Pax6, Olig2, Nkx2.2, and Isl1. (**K**) Significant differences in the peak of gene expression in the RT-qPCR experiments between mouse (orange) and human (blue). (human n = 3 in triplicate, mouse n = 3 in triplicate). Two-way ANOVA with Tukey's multiple comparison post-hoc test *** adj p-value < 0.001. (**K**) Time factor estimations for cluster pairs with high proportion of orthologous genes.

Figure 3. Dynamics of Shh signalling in mouse and human neural progenitors.

(**A**) Flow cytometry analysis of NKX6.1 expression in human NPs treated with the smoothened agonists SAG, purmorphamine (PM) or the two combined (both) shows a similar distribution of NKX6.1 expression at Day 2 and Day 4 (n = 3). (**B**) Scheme outlining the standard differentiation protocol, in which RA and SAG are added at the same time (light blue), versus a treatment where SAG addition is delayed for 24h (dark blue). (**C**) RT-qPCR data reveals higher expression of *IRX3* when cells are treated for 24h with only RA (dark blue), whereas there are no substantial differences in the induction dynamics *NKX6.1*, measured from the time of SAG addition (n = 3). (**D**) RT-qPCR data measured at 12h intervals reveal similar gene expression dynamics in mouse (orange) and human (blue) for Gli1, but distinct for Nkx6.1 (mouse n = 6, human n = 5). (a.u., arbitrary units).

Figure 4. Temporal control of gene expression depends on the species cellular environment.

(**A**) Scatter plot with histograms of PAX6 and NKX6.1 intensity measured by FACS in NPs from wt (orange) and hChr21 (purple) mouse cells at Day 2. (**B**) RT-qPCR expression of Olig2 from the mouse (*mOlig2*) and human alleles (*hOLIG2*) (n = 9). (**C**) smFISH at Day 2 of differentiation in wt and hChr21 lines with probes for *mSox2*, and allele specific detection of *mOlig2* or human *OLIG2* (*hOLIG2*). Scale bars = 10 microns (**D**) smFISH in human NPs at Day 8 of differentiation for *hSOX2* and *hOLIG2*. Scale bars = 50 microns. (**E**) Boxplots and density distributions in wt and hChr21 cells of number of mRNA molecules per cell from Sox2, total Olig2 and human- and mouse- allele specific probes. The estimated mean difference in molecule number between hChr21 cells and mouse is 25.7 [22.3; 29.7] (mouse n=323, hChr21 n=337). (**F**) Boxplots and density distributions of the concentration (number of mRNA

molecules per area unit) of Olig2 per cell in human NPs at Day 8, and mouse wt and hChr21 cells at Day 2. The estimated mean difference is 0.121 mRNAs/μm^2 [0.141; 0.101] between mouse and hChr21cells; and the mean difference is 0.157 mRNAs/μm^2 [0.175; 0.139] for human and hChr21 cells. Statistical significance (*) corresponds with <0.05 overlap between the distributions of mean estimations with a p-value for a two-sided permutation t-test < 0.001.(human n = 436, mouse n = 323, hChr21 n = 337).

Figure 5. Protein stability in the GRN corresponds to tempo differences between species.

(**A**) Normalized EU incorporation measurements to estimate mRNA half-life in mouse (orange) and human (blue) neural progenitors. Line and shadowed areas show best exponential fit and its 70% High Density Interval (HDI). (mouse Day 2 n = 5, human Day 4 n = 3, human Day 8 n = 5). (**B**) Half-life of the transcriptome in mouse neural progenitors at Day 2 (orange), and human neural progenitors at Day 4 (dark blue) and Day 8 (light blue). (**C**) Normalized AHA measurements of the proteome in mouse (orange) and human (blue) neural progenitors to estimate protein stability (mouse Day 2 n = 6, human Day 4 n = 4, human Day 8 n = 4). (**D**) Global stability of the proteome in mouse neural progenitors at Day 2 (orange), and human neural progenitors at Day 4 (dark blue) and Day 8 (light blue). Statistical significance (**) corresponds with <0.01 overlap between the distributions of parameter estimations. (**E**) Temporal dynamics of the computational model of the neural tube GRN in mouse, and the predicted human behaviour, simulated by halving the decay rates of the proteins of the network. Inset diagram of the cross-repressive GRN comprising the transcription factors Pax6, Olig2, Nkx2,2 and Irx3 used to model ventral patterning of the neural tube. (**F**) Predicted Olig2 time factor, indicating relative change in developmental pace, produced in response to fold changes in mRNA half-life and protein half-life. Relevant fold changes in mRNA and protein correspond to those that give a time factor of 2.5 (purple). (**G**) Predicted Olig2 time factor as a function of the fold change in the decay rate ratio (blue solid line). The change in time factor resulting from an increase in protein half-life grows faster than linearly (dashed line). This results in a time factor larger than 2 for a fold change of 2 in protein half-life (red line).

Figure 6. Protein decay and cell cycle account for the speed differences between species.

(**A**) Normalised measurements of mouse and human NKX6.1, OLIG2, SOX1 and SOX2 from AHA pulse-chase experiments using AHA-labeled and purified proteins. Line and shadowed areas show best exponential fit and 95% confidence intervals (mouse n = 3; human n = 3 for OLIG2 and NKX6.1, n = 4 for SOX1 and SOX2). (**B**) Normalized intensity measurements of mKATE2 in mouse and human Ptch1::T2A-mKate2 cell lines. Line and shadowed areas show best exponential fit and 70% HDI (mouse n = 7; human n = 4). (**C**) Estimated half-lives for mKATE2 in mouse (orange) and human (blue) cells**. (D)** Cell cycle measurements of mouse neural progenitors at Day 2, and human neural progenitors at Day 4 and Day 8. Line and shadowed areas show best fit and 80% HDI (mouse n=5, human Day 4 n= 4, human Day 8 n = 5). (**E**) Cell cycle length estimations in mouse neural progenitors at Day 2, and human neural progenitors at Day 4 and Day 8. For all plots, mouse data is orange-colored, and human is blue. Statistical significance (**) corresponds with <0.01 overlap between the distributions of parameter estimations.
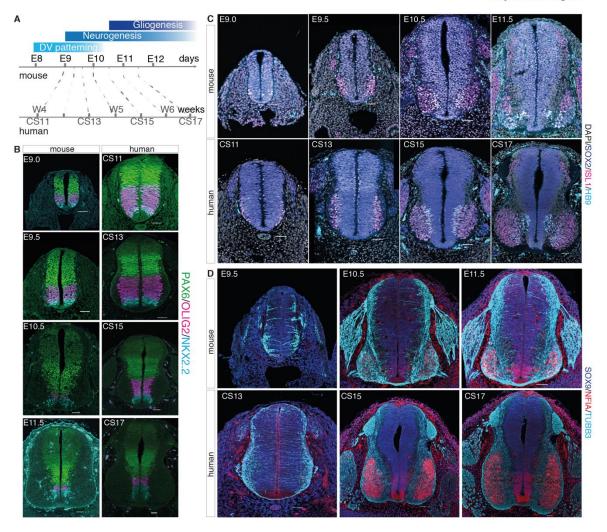
Figure 1. Comparison of neural tube development in mouse and human embryos.
(A) Schema of mouse and human neural tube development. **(B-D)** Immunofluorescence in transverse sections of mouse and human cervical neural tube from E9.0 to E11.5 in mouse and CS11 to CS17 in human embryos. **(B)** Expression of neural progenitor markers PAX6 (green), OLIG2 (magenta) and Nkx2.2 (cyan). **(C)** Pan-neural marker Sox2 (blue), motor neuron markers ISL1 (magenta) and HB9 (cyan) at neurogenic stages. **(D)** Early ventral expression of gliogenic markers NFIA (red) and SOX9 (blue) in the neural tube can be detected from E10.5 in mouse and CS15 in human. NFIA also labels neurons, as indicated by TUBB3 (cyan) staining. Scale bars = 50 microns.
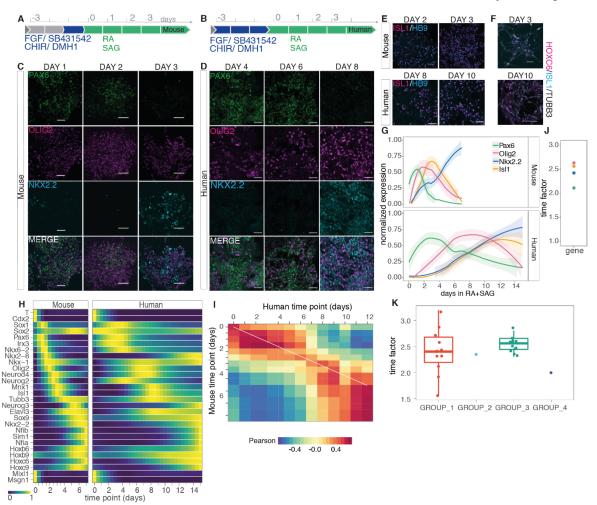
15

Figure 2. A global scaling factor for in vitro differentiations of mouse an human MNs.
(A) Schema of mouse ESCs differentiated to MNs. Spinal cord progenitors generated via an NMP state induced by the addition of FGF, WNT and dual SMAD inhibition signals for 24h (blue rectangle), subsequently exposed to the neuralizing signal retinoic acid (RA) and smoothened agonist (SAG) to ventralise the cells (green). **(B)** Schema of the analogous strategy used for human ESCs to generate MNs, where the addition of FGF, WNT and dual SMAD inhibition signals lasts 72h. **(C)** Expression of NP markers (PAX6, OLIG2, NKX2.2) between Days 1 and 3 in mouse MN differentiation. **(D)** Expression of NP markers (PAX6, OLIG2, NKX2.2) at Days 4, 6 and 8 in human MN differentiation. **(E)** Expression of MN markers (ISL1, HB9/MNX1) in mouse and human MNs. Mouse MNs can be detected by Days 2-3, whereas human MNs are not detected until Days 8 and 10. **(F)** HOXC6 expression in MNs characterized by ISL1 and TUBB3 expression at Day 3 in mouse and in human Day 10. Scale bars = 50 microns. **(G)** RT-qPCR analysis of Pax6, Olig2, Nkx2.2 and Isl1 expression in mouse and human differentiation reveals a conserved progression in gene expression but a different tempo (mouse n = 9, human n = 9). **(H)** Heatmap of RNA-seq data from mouse and human MN differentiation indicating the normalized expression of selected markers representative of neuromesodermal progenitors, neural progenitors, neurons, glia and mesoderm cell types (mouse n = 3, human n = 3). **(I)** Heatmap of pair wise Pearson correlation coefficients of the transcriptomes of mouse (vertical) and human (horizontal) differentiation at the indicated time points. High positive correlation indicated by values close to 1 (red). White line shows a linear fit of the Pearson correlation with temporal scaling factor of 2.5 ± 0.2 (median ± std). **(J)** Scaling factor for transcriptome clusters that contain Pax6, Olig2, Nkx2.2, and Isl1. **(K)** Time factor estimations for cluster pairs with high proportion of orthologous genes.
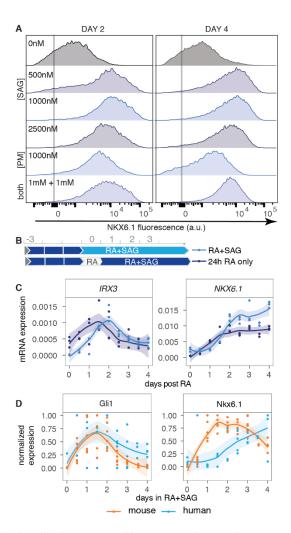
16

Figure 3. Dynamics of Shh signaling in mouse and human neural progenitors.
(A) Flow cytometry analysis of NKX6.1 expression in human NPs treated with the smoothened analogs SAG, purmorphamine (PM) or the two combined (both) shows a similar distribution of NKX6.1 expression at day 2 and 4 (n = 3). **(B)** Scheme outlining the standard differentiation protocol where RA and SAG are added at the same time (light blue), versus a treatment where SAG addition is delayed for 24h (dark blue). **(C)** RT-qPCR data reveals an earlier expression of *IRX3* when cells are treated for 24h with only RA (dark blue), whereas there are no substantial differences in the induction dynamics *NKX6.1*, measured from the time of SAG of addition (n = 3). **(D)** RT-qPCR data measured in 12h intervals reveals similar gene expression dynamics in mouse (orange) and human (blue) for Gli1, but distinct Nkx6.1 expression (mouse n = 6, human n = 5). (a.u., arbitrary units).
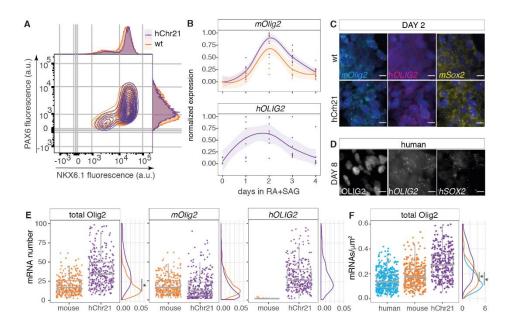
17

Figure 4. Temporal control of gene expression depends on the species cellular environment.
(A) Scatter plot with histograms of PAX6 and NKX6.1 intensity levels measured by FACS in NPs from wt (orange) and hChr21 (purple) mouse cells at Day 2. **(B)** RT-qPCR expression of Olig2 from the mouse (m*Olig2*) and human alleles (h*OLIG2*) (n = 9). **(C)** smFISH at Day 2 of differentiation in wt and hChr21 lines with probes for mSox2, and allele specific detection of m*Olig2* or human *OLIG2* (h*OLIG2*). Scale bars = 10 microns. **(D)** smFISH in human NPs at Day 8 of differentiation for h*SOX2* and h*OLIG2*. Scale bars = 50 microns. **(E)** Boxplots and density distributions in wt and hChr21 cells of number of mRNA molecules per cell from Sox2, total Olig2 and human- and mouse- allele specific probes. The estimated mean difference in molecule number between hChr21 cells and mouse is 25.7 [22.3; 29.7] (mouse n=323, hChr21 n=337). **(F)** Boxplots and density distributions of the concentration (number of mRNA molecules per area unit) of Olig2 per cell in human NPs at Day 8 and mouse wt and hChr21 cells at Day 2. The estimated mean difference is 0.121 mRNAs/μm^2 [0.141; 0.101] between mouse and hChr21cells; and the mean difference is 0.157 mRNAs/μm^2 [0.175; 0.139] for human and hChr21 cells. Statistical significance (*) corresponds with <5% of overlap between the distributions of mean estimations. (human n = 436, mouse n = 323, hChr21 n = 337).
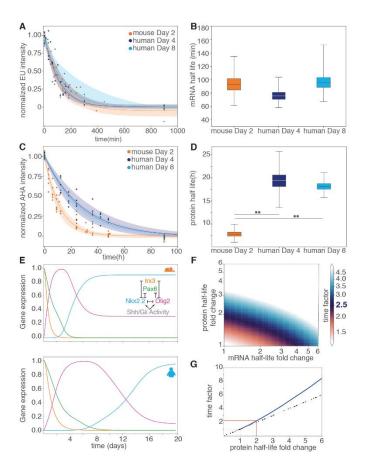
Figure 5. Protein stability in the GRN corresponds to tempo differences between species.
(A) Normalized EU incorporation measurements to estimate mRNA half-life in mouse (orange) and human (blue) neural progenitors. Line and shadowed areas show best exponential fit and its 70% High Density Interval (HDI). (mouse Day 2 n = 5, human Day 4 n = 3, human Day 8 n = 5). **(B)** Half-life of the transcriptome in mouse neural progenitors at Day 2 (orange), and human neural progenitors at Day 4 (dark blue) and Day 8 (light blue). **(C)** Normalized AHA measurements of the proteome in mouse (orange) and human (blue) neural progenitors to estimate protein stability (mouse Day 2 n = 6, human Day 4 n = 4, human Day 8 n = 4). **(D)** Global stability of the proteome in mouse neural progenitors at Day 2 (orange), and human neural progenitors at Day 4 (dark blue) and Day 8 (light blue). Statistical significance (**) corresponds with <1% of overlap between the distributions of parameter estimations. **(E)** Temporal dynamics of the computational model of the neural tube GRN in mouse, and the predicted human behaviour, simulated by halving the decay rates of the proteins of the network. Inset diagram of the cross-repressive GRN comprising the transcription factors Pax6, Olig2, Nkx2,2 and Irx3 used to model ventral patterning of the neural tube. **(F)** Predicted Olig2 time factor, indicating relative change in developmental pace, produced in response to fold changes in mRNA half-life and protein half-life. Relevant fold changes in mRNA and protein correspond to those that give a time factor of 2.5 (purple). **(G)** Predicted Olig2 time factor as a function of the fold change in the decay rate ratio (blue solid line). The change in time factor resulting from an increase in protein half-life grows faster than linearly (dashed line). This results in a time factor larger than 2 for a fold change of 2 in protein half-life (red line).
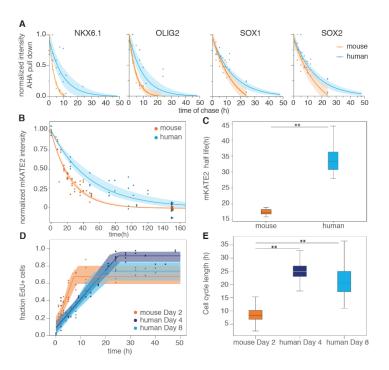
19

Figure 6. Protein decay and cell cycle account for the speed differences between species.
(A) Mouse and human normalized intensity measurements of NKX6.1, OLIG2, SOX1 and SOX2 decay after AHA pulse-chase experiments on AHA-labeled and purified nascent proteins. Line and shadowed areas show best exponential decay fit with its 95% confidence intervals (mouse n = 3; human n = 3 for OLIG2 and NKX6.1, n = 4 for SOX1 and SOX2). **(B)** Normalized intensity measurements of mKATE2 in mouse and human Ptch1::T2A-mKate2 cell lines. Line and shadowed areas show best exponential fit and its 70% HDI. **(C)** Estimated mKATE2 stability in mouse and human neural progenitors (mouse n = 7; human n = 4). **(D)** Cumulative fraction of EdU positive cells in mouse neural progenitors at Day 2, and human neural progenitors at Day 4 and Day 8. Line and shadowed areas show best fit and its 80% HDI (mouse Day 2 n = 5, human Day 4 n = 4, human Day 8 n = 5). **(E)** Cell cycle length estimations in mouse neural progenitors at Day 2, and human neural progenitors at Day 4 and Day 8. Statistical significance (**) corresponds with <1% of overlap between the distributions of parameter estimations.